Retrieval of Rain Rates for Tropical Cyclones From Sentinel-1 Synthetic Aperture Radar Images

Xianbin Zhao, Weizeng Shao, *Member, IEEE*, Zhengzhong Lai, and Xingwei Jiang

***Abstract*—The purpose of this study was to develop a method for retrieving the rain rate from C-band (∼5.3 GHz) synthetic aperture radar (SAR) images during tropical cyclones (TCs). Seven dual-polarized (vertical–vertical [VV] and vertical–horizontal [VH]) Sentinel-1 (S-1) SAR images were acquired in the interferometric-wide (IW) swath mode during the Satellite Hurricane Observation Campaign. These images were collocated with rain rates measured by the Stepped-Frequency Microwave Radiometers onboard National Oceanic and Atmospheric Administration aircraft. Wind speeds were retrieved from the VH-polarized SAR images using the geophysical model function (GMF) S1IW.NR. We determined the difference between the measured normalized radar cross section (NRCS) based on VV-polarized SAR and the predicted NRCS derived using the GMF CMOD5.N forced with wind speeds retrieved from VH-polarized SAR images. Rain cells were identified as regions in the images where the NRCS difference was greater than 0.5 dB or smaller than −0.5 dB. We found that the difference in the NRCS decreased and the VH-polarized wind speed increased with increasing rain rate. Based on these findings, we developed an empirical function for S-1 SAR rain retrieval in a TC, naming it CRAIN_S1. The validation of the CRAIN_S1 results with Tropical Rainfall Measuring Mission data resulted in a root mean square error of 0.58 mm/h and a correlation of 0.89. This study provides an alternate method for rain monitoring utilizing SAR data with a fine spatial resolution.**

***Index Terms*—Rain rate, synthetic aperture radar (SAR), tropical cyclones (TCs).**

I. Introduction

IT IS well known that rain is an essential factor in oceanography. It plays an important role in the energy exchange at the air–sea interface [1] and is especially important for predicting the tracks of tropical cyclones (TCs) [2], [3]. Rain observations in coastal waters are generally collected using a ship-based approach. However, this method is rarely applied for rain monitoring under high sea states, i.e., typhoons and hurricanes. Remote sensing is an advanced technology capable of observing rainfall over the global seas [4]. The meteorological Tropical Rainfall Measuring Mission (TRMM) was launched in 1997 by the National Aeronautics and Space Administration and the Japan Aerospace Exploration Agency. Although the TRMM is specially designed for quantitative measurement of tropical and subtropical rainfall with a spatial resolution of 0.25° (∼25 km) [5], TRMM data are too coarse for studying sea surface dynamics at the small (submesoscale) scale.

Synthetic aperture radar (SAR) is an active sensor that operates at microwave frequencies. It has the ability to conduct sea surface observations at all times and under all weather conditions [6]. Compared with real aperture radar, the spatial resolution of SAR at the azimuthal/flight direction is significantly better, e.g., 1 m pixel size for the German TerraSAR-X (TS-X) in the *X*-band [7] and for the Chinese Gaofen-3 (GF-3) in the C-band [8]. This improvement in resolution is due to the motion of water particles parallel to the satellite platform, i.e., the Doppler shift. However, the Doppler shift also renders sea surface waves with lengths larger than a specific value undetectable. This unique characteristic of SAR is referred to as velocity bunching [9]. Traditionally, low-to-moderate wind speeds can be operationally retrieved from co-polarization (vertical–vertical [VV] and horizontal–horizontal [HH]) SAR images using a well-developed geophysical model function (GMF). This function describes the empirical relationship between the SAR backscattering signal and the wind vector [10], e.g., the C-band model (CMOD) family for the C-band [11], the *X*-band model (XMOD) for the *X*-band [12], and the L-band model (LMOD) for the L-band [13]. The co-polarized SAR backscattering signal encounters a saturation problem at high wind speeds (>25 m/s) [14], [15]. Therefore, hurricane/typhoon winds are usually inverted from cross-polarization [vertical–horizontal (VH) and horizontal–vertical (HV)] SAR images [16], [17]. The effect of heavy rain on wind speed estimation has been discussed in several research reports [18], [19], [20], [21] that have concluded that heavy rain has a significant influence on co-polarized microwave backscattering. To address this issue, a few studies have developed approaches for TC wind retrieval from co-polarized scatterometers [22] and SAR [23] data. SAR wave retrieval methodology can be divided into two main categories: theoretical schemes based on the SAR mapping mechanism [24], [25], [26] and empirical models [27], [28]. Although these methods are suitable for SAR wave retrieval under regular sea states, wave retrieval during TCs is a challenge

Manuscript received 6 December 2022; revised 27 January 2023 and 18 February 2023; accepted 8 March 2023. Date of publication 13 March 2023; date of current version 6 April 2023. This work was supported in part by the National Natural Science Foundation of China under Grant 42076238, Grant 42176012, and Grant 42130402, and in part by the Natural Science Foundation of Shanghai under Grant 23ZR1426900. *(Corresponding author: Weizeng Shao.)*

Xianbin Zhao is with the College of Meteorology and Oceanography, National University of Defense Technology, Changsha 410073, China (e-mail: zxb15951944015@163.com).

Weizeng Shao is with the College of Marine Sciences, Shanghai Ocean University, Shanghai 201306, China, and also with the National Satellite Ocean Application Service, Shanghai 201306, China (e-mail: swz19@tsinghua.org.cn).

Zhengzhong Lai is with the Shanghai Ocean University, Shanghai 201306, China (e-mail: m210200591@st.shou.edu.cn).

Xingwei Jiang is with the Shanghai Ocean University, Shanghai 201306, China, and also with the Southern Marine Science and Engineering Guangdong Laboratory (Guangzhou), Guangzhou 511458, China (e-mail: xwjiang@mail.nsoas.org.cn).

Digital Object Identifier 10.1109/JSTARS.2023.3255922

because the SAR backscattering is distorted by the effects of velocity bunching.

A few clusters on the SEASAT SAR have been identified as rainfall footprints [29], [30]. During storms, rain cells are clearly observed by spaceborne SAR [31], [32] at high incidence angles, but the pattern of the rain cells is generally less apparent at low incidence angles. Rain cells affect the SAR backscattering signal through three mechanisms [33]: turbulence or damping of small-scale waves produced by winds [34]; various splash products generated by raindrops such as ring waves, stalks, and crowns [35], [36]; and enhancement of the roughness caused by downdrafts of large-scale wind flow associated with raindrops [37]. Although these phenomena contribute to the SAR roughness, ring waves are assumed to be the dominant feature in the co-polarization channel [38]. In our recent study [39], ring waves with a wavelength of less than 125 m were clearly observed in the SAR-derived wave spectra. Because rain-induced backscattering dominates the sea surface backscattering in moderate to heavy rains, a scatterometer-derived rain GMF [34], [35] for three different incidence angle ranges was developed using HH-polarized RADARSAT-1 (R-1) scanning SAR (ScanSAR) images collocated with NEXRAD data. Although this approach has been implemented for coarse-resolution SAR (i.e., a 500 m pixel size for R-1 ScanSAR), a more complicated rain retrieval GMF will be needed for fine-resolution SAR at wide incidence angles.

Mastenbroek and de Valk [25] determined that the TRMM rain rate is linearly correlated with the difference between the SAR-measured normalized radar cross section (NRCS) and an NRCS simulated using a theoretical SAR backscattering model based on GF-3 SAR images acquired during TCs. Therefore, we developed a rain retrieval algorithm based on several dual-polarized Sentinel-1 (S-1) SAR images acquired during TCs with wind speeds of up to 70 m/s. These images were acquired in the interferometric-wide (IW) swath mode. The sea state during TCs is complicated, with high winds, extreme waves, strong currents, and breaking waves. In the literature, the SAR-measured NRCS consists mainly of resonant Bragg-wave backscattering modulated by the wind, waves, and current [40], and a non-Bragg (NB) scattering component caused by breaking waves [41], [42]. In this study, the sea state during a TC was simulated using a numeric wave model WAVEWATCH-III (WW3) [43], in which winds from the European Centre for Medium-Range Weather Forecasts (ECMWF) reanalysis data (ERA-5) and the sea surface current from the hybrid coordinate ocean model (HYCOM) are treated as the forcing field [44]. Using the model-simulated sea state and the HYCOM current, an improved composite surface radar backscattering model based on the Bragg scattering theory was used to calculate the resonant NRCS component at moderate incidence angles [45], [46]. The NB contribution was estimated using an empirical function [47] and by taking the SAR-derived winds obtained from a VH-polarized S-1 SAR image using a GMF (i.e., the S-1 IW mode wind speed retrieval model after noise removal, S1IW.NR) [48]. We observed a difference between the observed NRCS and the simulated NRCS in the rain cells forming the basis for the rain rate retrieval algorithm we developed.

The remainder of this article is organized as follows. The datasets, i.e., the dual-polarized S-1 SAR images, ERA-5 wind fields, HYCOM sea surface currents, rain rate measurements from the Stepped-Frequency Microwave Radiometers (SFMRs) onboard National Oceanic and Atmospheric Administration (NOAA) aircraft, the TRMM rain data, and the settings of the WW3 model, are introduced in Section II. Section III describes the methodology of the SAR roughness simulation, NB estimation, and rain cell identification. Section IV presents the results of the rain cell identification and rain rate retrieval. This section also presents the validation of the rain rate against the SFMR observations. Section V concludes this article.

TABLE I
INFORMATION FOR COLLECTED SENTINEL-1 (S-1) SAR IMAGES ACQUIRED IN THE IW SWATH MODE IN TROPICAL TYPHOONS, WITH A PIXEL SIZE OF 40 M (80 M SPATIAL RESOLUTION) AND INCIDENCE ANGLES OF 30°–50°

Cyclone ID	Acquisition time	Cyclone Eye (°E, °N)	Central Pressure (hPa)	Maximum Wind Speed (m/s)
Hermine	2016/09/01 23:45 UTC	275.2, 29.0	983	35.98
Lionrock	2016/08/29 08:32 UTC	142.7, 31.3	950	41.12
Irma	2017/09/07 10:30 UTC	291.0, 20.2	921	74.53
Maria	2017/09/23 10:44 UTC	287.9, 25.1	952	51.4
Dorian	2019/08/30 22:46 UTC	288.9, 25.3	949	59.11
Isaias	2020/08/02 23:19 UTC	280.3, 28.2	995	30.84
Delta	2020/10/08 00:07 UTC	269.8, 22.3	973	41.12

II. DESCRIPTION OF DATASET

A. SAR Images

Seven dual-polarized (VV and VH) S-1 SAR images produced as a Level-1 product were obtained from the Satellite Hurricane Observation Campaign (SHOC). These images were acquired in the IW swath mode in both the azimuthal and range directions with a pixel size of 40 m (80 m spatial resolution) and incidence angles of 30°–50°. Information about the images is listed in Table I. The collected images in VV polarization are shown in Fig. 1.

B. Rain Data

During the hurricane season, synchronous wind and rain measurements are collected by SFMR following the flight of the NOAA aircraft [see the red line in Fig. 1(c)]. The TRMM data are a valuable remote-sensed source for studying the climatology of tropical precipitation variability [49]. The spatial resolution of the rainfall rate data measured by the TRMM satellite is 0.25° grids, with an interval of 3 h. It should be noted that SFMR observations (largely the wind speed and rain rate) were available for four of the images (Hurricanes Maria, Lionrock, Hermine, and Isaias), whereas the other images were collocated with TRMM rain data (Hurricanes Irma, Dorian, and Delta). In this study, the SFMR measurements were used to develop an SAR rain retrieval algorithm, and the SAR-derived rain rate was validated against the TRMM data. Due to insufficient TRMM

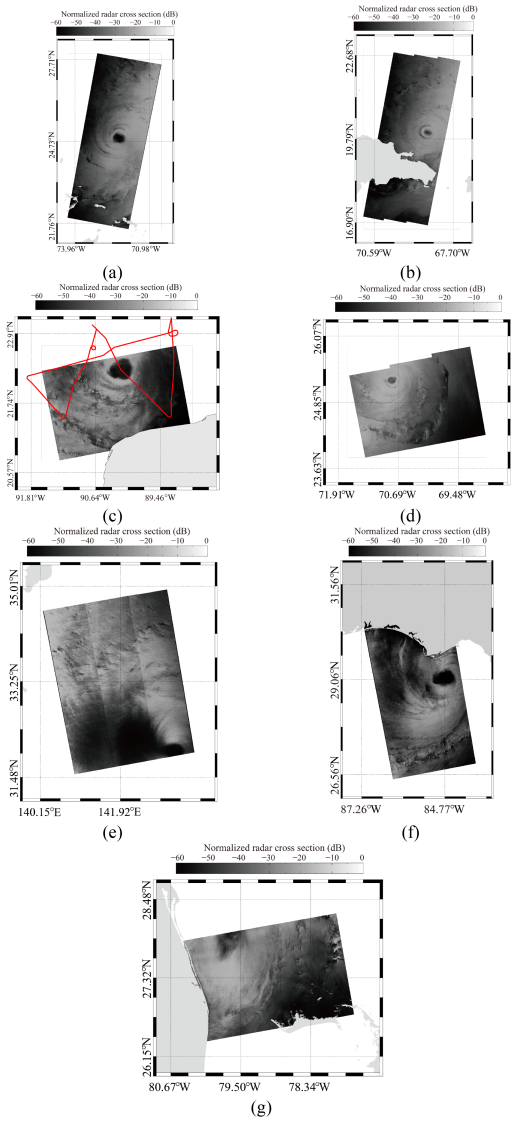

Fig. 1. VV-polarized Sentinel-1 (S-1) images acquired in the IW swath mode of seven hurricanes. (a) Hurricane Maria at 10:44 UTC on September 23, 2017. (b) Hurricane Irma at 10:30 UTC on September 7, 2017. (c) Hurricane Delta at 00:07 UTC on October 8, 2020. (d) Hurricane Dorian at 22:46 UTC on August 30, 2019. (e) Hurricane Lionrock at 08:32 UTC on August 29, 2016. (f) Hurricane Hermine at 23:45 UTC on September 1, 2016. (g) Hurricane Isaias at 23:19 UTC on August 2, 2020. The red lines denote the tracks of the SFMR.

data collocated with SFMR observations, a comparison between the TRMM and SFMR is not made in this work. However, the SFMR observations are well-calibrated and have been used in research on SAR wind retrieval [48]. Fig. 2 shows the TRMM rain map of Hurricane Maria [corresponding to Fig. 1(a)] in which the rain band around the cyclone's center is apparent and has a rain rate of up to 10 mm/h.

C. Hindcast Waves From WW3 Model

Information about the sea state is required to simulate the SAR sea surface roughness. However, extreme wave retrieval during a TC is a challenge because the SAR roughness is modulated by currents, breaking waves, and rainfall [50]. Therefore, the sea states during TCs were simulated using a third-generation numeric wave model, i.e., WW3. The ERA-5 data, with 0.25°

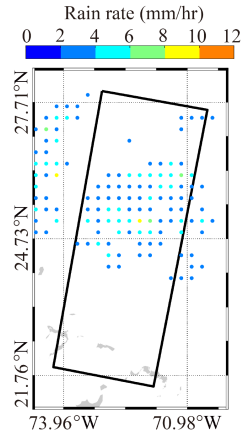

Fig. 2. TRMM rain maps during Hurricane Maria corresponding to the image in Fig. 1(a).

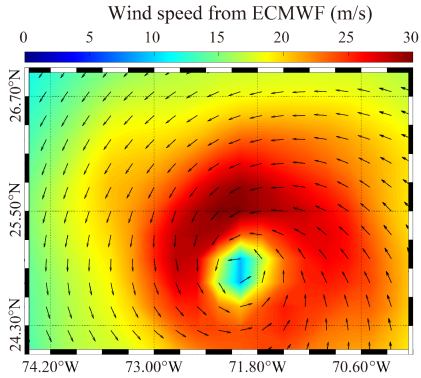

Fig. 3. ECMWF reanalysis data (ERA-5) wind map during Hurricane Maria on September 23, 2017 at 10:00 UTC.

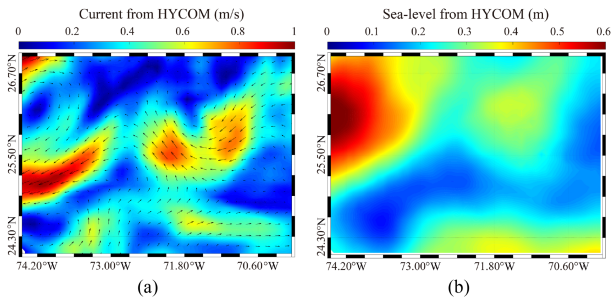

Fig. 4. HYCOM (a) current and (b) sea-level maps during Hurricane Maria on September 23, 2017 at 09:00 UTC.

grids and an interval of 3 h, were used as the forcing field. The water depth data from the bathymetric topography of the General Bathymetry Chart of the Oceans (GEBCO) has a 1 km horizontal resolution. The ERA-5 wind map for September 23, 2017 at 10:00 UTC during Hurricane Maria is shown in Fig. 3. As was determined in earlier research [51], wave simulations of typhoons are influenced by high wind-induced currents and sea level rise. Sea surface current and sea-level data from HYCOM with a 1/12° (∼8 km) grid spatial resolution and a 1-h interval were collected simultaneously and used as the forcing field in the WW3 model. The HYCOM current and sea-level maps for September 23, 2017 at 09:00 UTC during Hurricane Maria

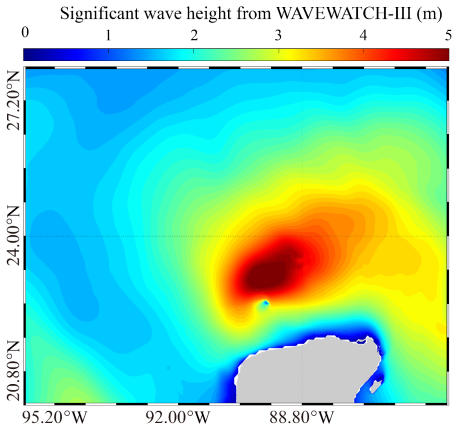

Fig. 5. Map of the SWH from the WAVEWATCH-III (WW3) model during Hurricane Delta on October 8, 2020 at 00:07 UTC.

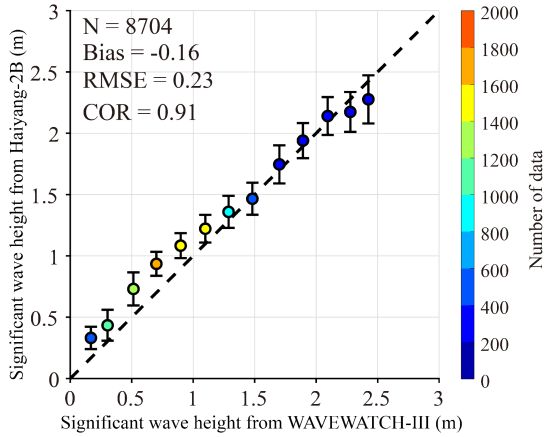

Fig. 6. Statistical analysis of the correlation between the WW3-simulated SWH and the measurements from the Hiayang-2B (HY-2B) altimeter.

are shown in Fig. 4(a) and (b), respectively. The details of the settings of the WW3 model are described as follows.

1) The simulated regions included the entire track and occurrence for each TC using rectangular grids.
2) The 2-D wave spectrum was resolved into 24 regular azimuthal directions with a 15° step, and the computation step was set as 300 s time steps in both the longitudinal and latitudinal directions.
3) The frequency bins were logarithmic and ranged from 0.04118 to 0.7186 at an interval of $\Delta fff = 0.01$.
4) The spatial resolution of the simulated wave spectrum was set at 0.05° grid with an interval of 30 min.
5) The parameterizations of switches ST2 and STAB2 for the input/dissipation terms [22] and the four wave components (quadruplets) of the wave–wave interactions followed the generalized multiple discrete interaction approximation [17].

The HY-2B altimeter was specifically designed for global wave monitoring, even during TCs. Currently, some satellites, e.g., Jason-2 [52] and the Chinese Haiyang-2B (HY-2B), provide a wave product following the footprint of their flight with a ∼0.3 m root mean square error (RMSE) for significant wave height (SWH) under low-to-moderate sea states (SWH $<$ 7 m) [53]. Therefore, available measurements from the HY-2B altimeter were used to validate the WW3 simulated during the duration of Hurricanes Dorian, Isaias, and Delta. However, HY-2B wave data were not available for the duration of the other TCs. Fig. 5 shows the case map of the WW3-simulated SWH of Hurricane Delta on October 8, 2020 at 00:07 UTC. The statistical analysis yielded an RMSE of 0.23 and a correlation coefficient (COR) of 0.91 (see Fig. 6) with an SWH of up to 3 m, indicating that the use of WW3-simulated waves in this study was reliable.

III. Methodology

In this section, the sea surface backscattering model for simulating the SAR roughness [54] is described, including the wind, wave, and current terms. In particular, the empirical model for the NB estimation caused by wave breaking is introduced. Then, the method of rain cell identification in the images is presented using VV- and VH-polarized SAR winds. Finally, the empirical algorithm of rain retrieval is proposed.

The process for retrieving the rain rate from dual-polarized S-1 IW SAR is illustrated in Fig. 7.

A. SAR Backscattering Model

SAR backscattering returns depend on sea surface roughness due to gravity-capillary Bragg resonant waves and wave-induced NB backscattering. Over the last few decades, the use of advanced radar backscattering to calculate and simulate the NRCS of the ocean surface at moderate incidence angles has become well developed. These methods incorporate wave-current interactions and the upwind/downwind differences in the NRCS [55]. Traditionally, the normalized Bragg wave resonant contribution σ_0 is defined as the average of the radar backscattering cross section (RCS) σ in the horizontal x and vertical y directions

$$\sigma_0 = \frac{\iint \sigma dx\, dy}{xy}. \tag{1}$$

The relationship between the RCS σ and the dimensional wave spectrum E is as follows:

$$\sigma = \mathrm{w}\sigma_0^P\ E(k_b, \varphi_b) \tag{2}$$

where

$$k_b = 2k_0\sqrt{\sin^2(\theta - S_p) + \cos^2(\theta - S_p)\sin^2(S_t)} \tag{3}$$

$$\varphi_\mathrm{b} = \varphi + \tan^{-1}\frac{\cos(\theta - S_p)\sin(-S_t)}{\sin(\theta - S_p)} \tag{4}$$

$$w = \frac{\cos(\theta - S_p)}{\cos\theta \times \cos S_p} \tag{5}$$

In (2)–(5), k_b is the wave number of the resonant Bragg waves related to the radar wave number k_0 (e.g., 5.3 cm for GF-3 and 3.1 cm for TS-X), φ_b is the direction of the Bragg waves, and w is the weighting function of the Bragg scattering. This accounts for the geometric modulation caused by the elevation or tilt toward the radar antenna, and it has a larger effective area for the radar than a horizontal facet of the same x and y dimensions within the reference plane. σ_0^P is the Bragg scattering in the co-polarization

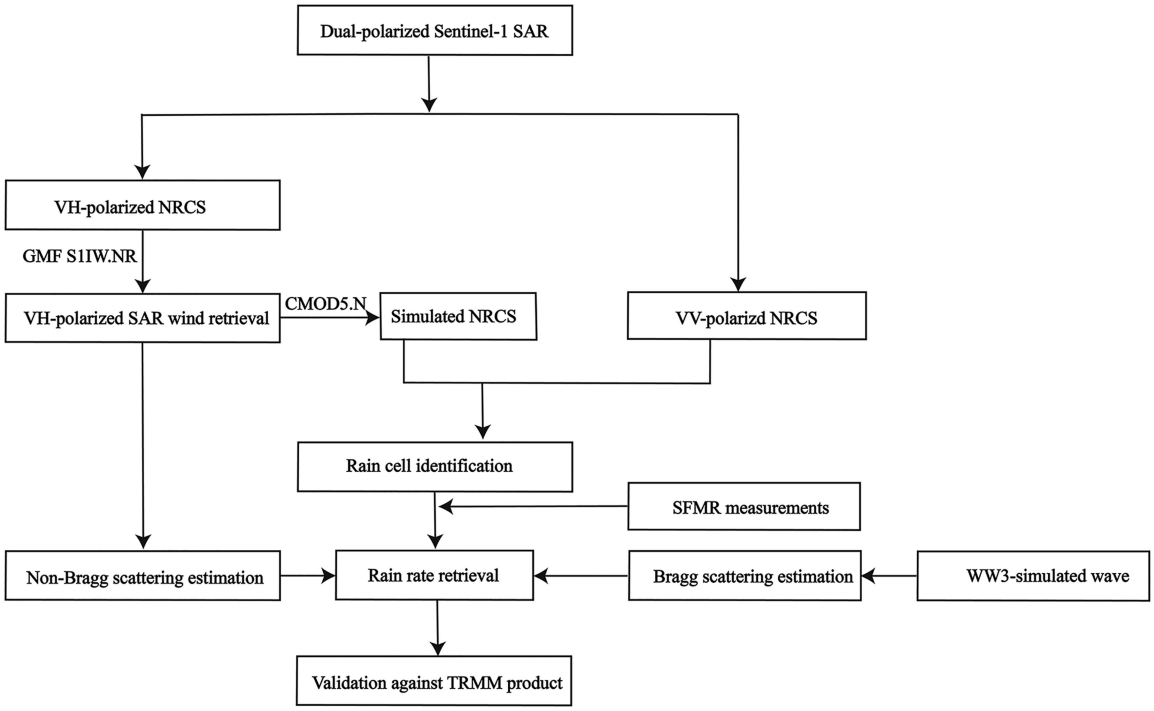

Fig. 7. Process for retrieving rain rate from the S-1 IW SAR.

channels (i.e., P denotes HH or VV polarization), θ is the incidence angle, φ is the radar look direction vertical to the flight platform, and S_p and S_t are the slopes of the tilted Bragg scattering facets parallel and vertical to the radar look direction, respectively. It should be noted that RCS σ is assumed to be an invalid value, and d is the filter threshold (value of 0.25) when $4\sin^2(\theta\text{-}S_p) < d^2$.

The Bragg scattering σ_0^P is calculated as follows:

$$\sigma_0^P = 8\pi k_0^4 \cos^4\theta_i \times \left| \left(\frac{\sin(\theta - S_p)\cos S_t}{\sin\theta_i} \right)^2 b_{PP} + \left(\frac{\sin S_t}{\sin\theta_i} \right)^2 b_{QQ} \right|^2 \tag{6}$$

where

$$b_{\mathrm{HH}} = \frac{\varepsilon}{\left(\cos\theta_i + \sqrt{\varepsilon}\right)^2} \tag{7}$$

$$b_{\mathrm{VV}} = \frac{\varepsilon^2(1+\sin^2\theta_i)}{\left(\varepsilon\cos\theta_i + \sqrt{\varepsilon}\right)^2}. \tag{8}$$

In (6)–(8), ε is the permittivity of seawater. PP and QQ denote the co-polarization option (VV or HH): if PP is set as VV, b_{PP} is the scattering coefficient for VV polarization b_{VV}, and QQ is the scattering coefficient for HH-polarization b_{HH}. θ_i is the effective incidence angle; that is, the radar incidence angle θ modulated by the slopes S_p and S_t.

$$\theta_i = \cos^{-1}\left[\cos(\theta - S_p) \times \cos S_t\right] \tag{9}$$

where

$$S_p = \tan^{-1}\left(\cos\varphi\frac{\partial\zeta}{\partial \mathrm{x}} + \sin\varphi\frac{\partial\zeta}{\partial \mathrm{y}}\right) \tag{10}$$

$$S_t = \tan^{-1}\left(-\sin\varphi\frac{\partial\zeta}{\partial \mathrm{x}} + \cos\varphi\frac{\partial\zeta}{\partial \mathrm{y}}\right). \tag{11}$$

The slopes S_p and S_t are a function of the sea surface elevation ζ in the radar look direction φ, and they are modulated by the waves and currents. Collectively, according to the above theoretical rationale, the NRCS is conveniently predicted using four parameters: 1) the wave energy spectrum; 2) the current speed; 3) the radar incidence angle; and 4) the radar azimuth angle. In this study, the wave energy spectrum during the TC was derived by hindcasting using the WW3 model. The HYCOM current was applied directly.

B. NB Estimation

According to its theoretical principle, the NB contribution can be calculated using a dual-polarized (VV and HH) SAR image [56]. However, S-1 SAR images are available only for the VV and VH polarization channels. In a recent study [47], more than 1000 quad-polarized RADARSAT-2 (R-2) SAR images were collocated with measurements from National Data Buoy Center buoys monitored by NOAA. It was found that the NB contribution is exponentially related to the wind speed. Wave breaking is determined by fetch, which is correlated with the sea surface wind speed U_{10}. In practice, the NB contribution σ_{wb} in the co-polarized SAR NRCS is as follows:

$$\sigma_{\mathrm{wb}} = F(\theta)Y(\varphi)U_{10}^{B(\theta)} \tag{12}$$

where

$$F(\theta) = 0.00019\mathrm{e}^{-0.32\times(\theta-30^\circ)} \tag{13}$$

$$B(\theta) = 1.3 + 0.047 \times (\theta - 30^\circ) \tag{14}$$

$$Y(\varphi) = \exp(a_0 + a_1\cos\varphi + a_2\cos 2\varphi) \quad (15)$$

$$a_0 = 0.24 - 0.014 \times (\theta - 30^\circ) \quad (16)$$

$$a_1 = 0.33 + 0.013 \times (\theta - 30^\circ) \quad (17)$$

$$a_2 = 0.12 + 0.014 \times (\theta - 30^\circ). \quad (18)$$

In (12)–(18), θ is the radar incidence angle and φ is the azimuth angle following the flight platform. Although σ_{wb} can be easily calculated when the sea surface wind speed U_{10} is known, the empirical approach does not require the HH and VV polarized SAR images. As was previously mentioned, the wind speed U_{10} is necessary for the NB estimation; therefore, the cyclonic winds were inverted from the VH-polarized S-1 SAR images, which were used in the above model.

C. Rain Cell Identification

The entire SAR image was divided into 128 × 128 pixel (azimuth × range) subscenes with a spatial coverage of 5 × 5 km to match the image with the WW3-simulated waves and HYCOM currents. The winds were retrieved from the VH-polarized S-1 image using GMF S1IW.NR [48]. Next, the VV-polarized NRCS was simulated using CMOD5.N [11] and the VH-polarized SAR winds. We determined that the wind directions were prior information in the CMOD5.N. Although the wind directions can be estimated from the homogenous pattern on the SAR image corresponding to the wind-induced low-frequency features of the SAR intensity spectrum [57], these features are distorted by high sea states and breaking waves. Regardless, the spectrum-based method is usually implemented for about 30% of acquisitions of S-1 IW swath mode under a moderate sea state [58]. In this sense, cyclonic winds with a spiral direction and an inflow angle of 20° in the polar coordinate system were used [59].

Due to the significant attenuation effect of rainfall on VV-polarized SAR images, we assumed that the difference between the simulated NRCS and the SAR-measured NRCS in the VV-polarized channel was produced by rain cells. The method for rain cell identification involved calculating the threshold value, which was proposed by Shen et al. [60]. The threshold value was set as follows:

$$\text{Value} = \sigma_0^{\mathrm{VV}} - \sigma_0^{\mathrm{CMOD5N}}\,[\mathrm{dB}] \quad (19)$$

where σ_0^{VV} is the observed NRCS (dB) and $\sigma_0^{\mathrm{CMOD5N}}$ is the NRCS simulated using CMOD5.N. In this study, the threshold value was assumed to be ±0.5 dB, that is, the values greater than 0.5 dB or smaller than −0.5 dB are identified as rain cells.

D. Rain Retrieval

The dataset included more than 1000 matchups with rain rates measured by the SFMR. We analyzed the relationships between the difference in the NRCS and the VH-polarized wind speed and the SFMR rain rate at incidence angles of 30°–50°. It should be noted that data for rain rates of <2 mm/h were excluded due to the occurrence of a few disturbances of the sea roughness induced by the small amount of rain. Fig. 8(a) and (b) shows the analysis results within a distance of 100 km from the cyclones' eyes. For incidence angles of 30°–50° with a 5° interval, the difference in the NRCS decreases with increasing rain rate, while the VH-polarized wind speed increases significantly with increasing rain rate. However, this type of behavior is relatively weak due to the smaller amount of precipitation beyond 100 km from the cyclones' eyes [see Fig. 8(c) and (d)].

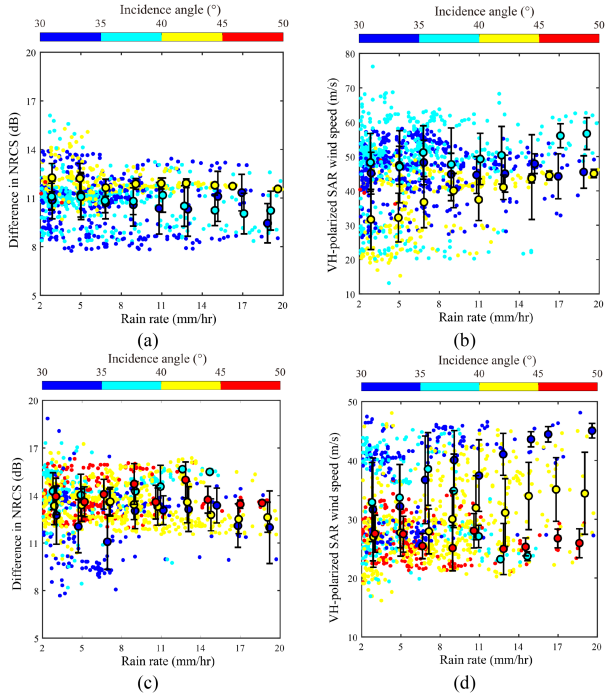

Fig. 8. Relationships between the SFMR rain rate and two variables: (a) Difference in the NRCS within a distance of 100 km from the cyclones' eyes. (b) VH-polarized SAR wind speed within a distance of 100 km from the cyclones' eyes. The relationship between the SFMR rain rate and two variables: (c) difference in the NRCS beyond a distance of 100 km from the cyclones' eyes and (d) VH-polarized SAR wind speed beyond a distance of 100 km from the cyclones' eyes.

As mentioned in [35], the rain-induced component in NRCS is expressed as a polynomial function of rain rate without considering the sea state. Based on the above findings, the rain rate is related to several factors of SAR. Therefore, a function referring to the empirical model CWAVE for SAR wave retrieval was constructed for rain rate retrieval from SAR images, denoted as CRAIN_S1 [28]

$$R = a_0 + \sum_{i}^{n} a_i \times s_i + \sum_{i,j=1}^{n} a_{i,j} \times s_i \times s_j \quad (20)$$

where R is the rain rate (mm/h); the imaging parameters s_i include the difference in the NRCS σ_{d} (dB), the incidence angle θ (30° to 50° with an interval of 5°), and the VH-polarized wind speed U_{10}; and $a_{i,j}$ is a coefficient vector determined by matchups by using the least square regression. It should be noted that CRAIN_S1 is specifically adopted within and beyond 100 km from the cyclones' eyes. Table II lists the coefficients of CRAIN_S1, in which the subscripts 1, 2, and 3 represent the variables σ_{d}, θ, and U_{10}, respectively, e.g., a_{12} is the coefficient for the term $\sigma_{\mathrm{d}} \times \theta$. Fig. 9 compares the simulated values of CRAIN_S1 with the SFMR rain rate data, yielding a 1.41 mm/h RMSE and a 0.82 COR.

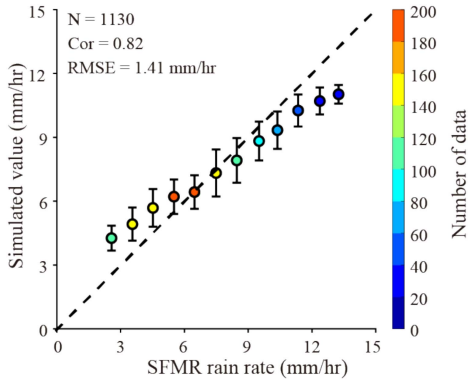

Fig. 9. Comparison of the values simulated using CRAIN_S1 and the SFMR rain rates.

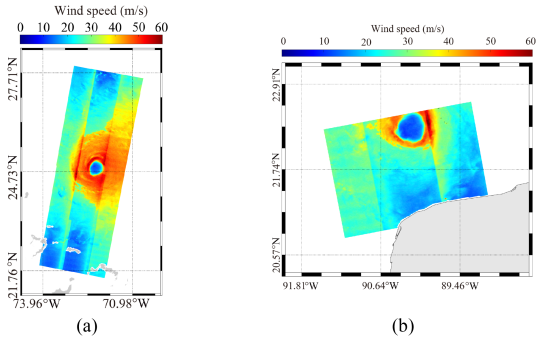

Fig. 10. Maps of the VH-polarized SAR winds obtained using GMF S1IW.NR. (a) Hurricane Maria at 09:00 UTC on September 23, 2017. (b) Hurricane Delta at 00:07 UTC on October 8, 2020.

IV. Results

As was mentioned by Shi et al. [61], the rain rate is correlated with the difference in the SAR roughness during TCs after removing the influence of the Bragg resonant component. The Bragg resonant component in the NRCS was calculated using the profiles, including the VH-polarized SAR-derived wind, HYCOM current, and WW3-simulated waves. An empirical model was implemented to calculate the NB component using the VH-polarized SAR-derived wind and the radar incidence angle and azimuth angle corresponding to the disturbance of the rain cells. Fig. 10 shows maps of the VH-polarized SAR winds corresponding to the images in Fig. 1, i.e., (a) Hurricane Maria and (b) Hurricane Delta. Noted that the large values in wind speed along the subswaths is caused by the noise, although the noise removals have been made in the cross-polarized GMFs. It was assumed that the difference between the observed NRCS and the sum of the Bragg resonant and NB component was induced by rain cells. The map of the simulated VV-polarized NRCS at 10:44 UTC on September 23, 2017, obtained by combining the Bragg resonant component with the NB component, is shown in Fig. 11(a) and (b) shows the difference between the sum of simulated NRCS and SAR-measured NRCS. Fig. 12 shows the map of the rain cell identification. This figure shows additional detail of the rain cells compared with the TRMM map in Fig. 2, especially at the rain wall around the cyclone eye. We

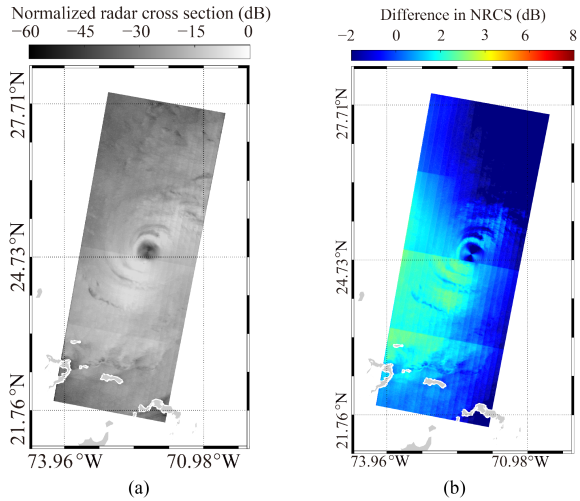

Fig. 11. (a) Map of the simulated VV-polarized NRCS at 10:44 UTC on September 23, 2017, obtained by combining the Bragg resonant component with the NB component induced by weak breaking. (b) Difference between the sum of simulated NRCS by theoretical approach and SAR-measured NRCS.

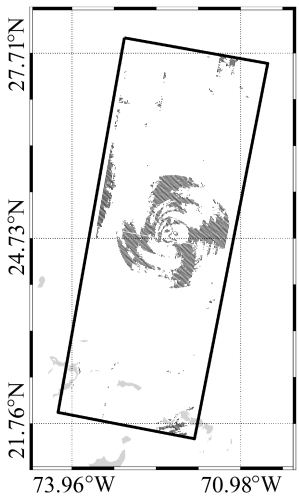

Fig. 12. Map of the rain cell identification during Hurricane Maria corresponding to the image in Fig. 1(a).

determined that the pattern of the rain cells was consistent with the TRMM data.

In the validation dataset, about 100 matchups with TRMM data were available for the three cyclones. The SAR-derived rain rate for the S-1 SAR image acquired at 10:44 UTC on September 23, 2017, during Hurricane Maria, is shown in Fig. 13. In addition, we applied CRAIN_S1 to three S-1 SAR images acquired during TCs and compared the retrieval results with the rain rate product of the TRMM. In Fig. 14, the RMSE of the rain rate is 0.58 mm/h and the COR is 0.89 (with rain rates of up to 8 mm/h). This indicates that the CRAIN_S1 algorithm can be applied for rain rate retrieval from dual-polarized S-1 SAR images acquired during TCs. However, it is necessary to verify that there are no available TRMM data for extreme rain rates of $>$20 mm/h in the validation procedure, indicating that the effectiveness of the proposed method needs to be further studied. Thus, the accuracy of the retrieval results obtained using CRAIN_S1 is expected to be

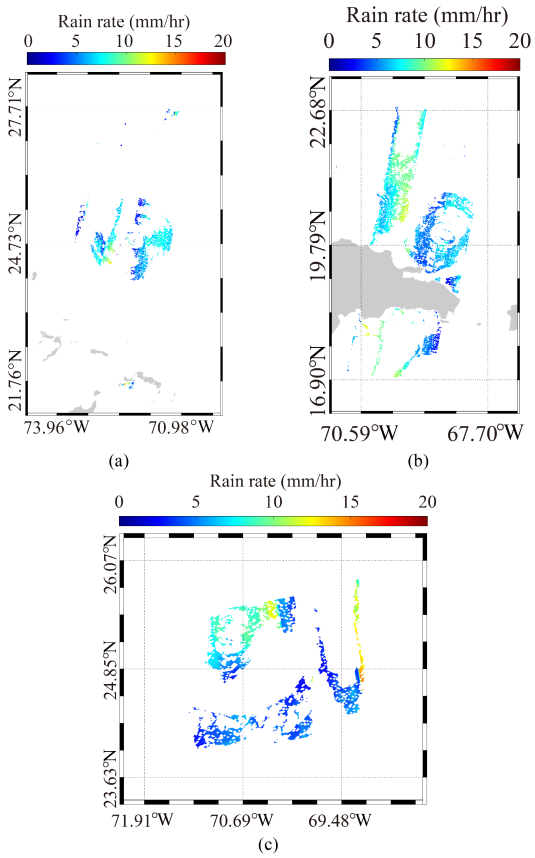

Fig. 13. SAR-derived rain rate for the S-1 SAR image acquired. (a) Hurricane Maria at 10:44 UTC on September 23, 2017. (b) Hurricane Irma at 10:30 UTC on September 7, 2017. (c) Hurricane Dorian at 22:46 UTC on August 30, 2019.

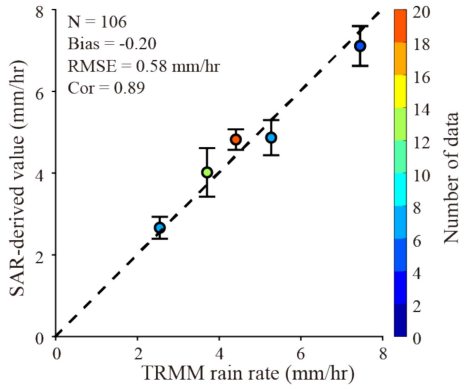

Fig. 14. Comparison of the retrieval results of CRAIN_S1 with the TRMM rain rate in the validation dataset.

further improved through abundant datasets with a wide range of incidence angles and heavy rainfall to enhance the applicability of the empirical model for NB estimation during TCs.

V. Conclusion

In the field of remote sensing, algorithms for wind and wave retrieval from co-polarized SAR images are readily available for use under low-to-moderate sea states ($U_{10} < 20$ m/s). Utilizing SAR backscattering in the cross-polarization channel, strong winds during TCs have also been inverted using cross-polarized GMFs, a process that can be practically implemented using data from various C-band SAR sensors. Although the effect of rain on the SAR roughness has been investigated and the characteristics of its effect on C- and *X*-band SAR have been studied, a quantitative approach for SAR rain retrieval from SAR images has been lacking. In this study, an analytical approach for SAR rain rate retrieval was developed.

We obtained seven S-1 SAR IW images from the dual-polarization channel (VV and VH) of the SHOC. Of these images, four images in Hurricanes Maria, Lionrock, Hermine, and Isaias were collocated with rain observations from the SFMR and were used to develop a rain rate retrieval algorithm. The remaining three images of Hurricanes Irma, Dorian, and Delta were used to validate the SAR-derived rain rate against TRMM data. The wind field was inverted from the VH-polarized image using the GMF S1IW.NR, which was then input into the GMF CMOD5.N to simulate the VV-polarized NRCS. The difference between the CMOD5.N-simulated and SAR-measured NRCS was calculated, and rain cells were identified as cells with values greater than 0.5 dB or smaller than −0.5 dB. The rain cell identification results are more detailed than the calibrated TRMM products.

The Bragg resonant component related to strong wind, waves, and current during a TC was obtained using a polarimetric microwave radar backscatter model. The NB contribution induced by wave breaking was estimated using an empirical model. We found that the SFMR rain rate had a linear correlation with the difference in the NRCS (values measured with SAR minus the composite values of the Bragg resonant and NB component) and the VH-polarized wind speed. Therefore, an empirical function was derived for SAR rain rate retrieval and specifically tuned for distances within and beyond 100 km from the eye of the TC. The fitting results were compared with SFMR measurements, yielding a COR of 0.82 for the rain rate. The validation against the TRMM data yielded an RMSE of 0.58 mm/h for the rain rate, with rain rates of up to 8 mm/h. In conclusion, the proposed approach is a promising technique for SAR rain monitoring during TCs, although this method relies on the model-simulated wave spectrum and has limitations outside of the TC eye due to the weak relationship between the difference in NRCS and rain rate.

In the near future, more images with wide range incidence angles and high rain rates will be obtained and the empirical model for NB estimation will be adapted for high sea states to improve the accuracy of SAR rain retrieval.

Acknowledgment

The authors greatly appreciate the provision of the Sentinel (S-1) synthetic aperture radar (SAR) images by the European Space Agency via https://scihub.copernicus.eu and the provision of the source code for the WAVEWATCH-III model free of charge by the National Centers for Environmental Prediction of the National Oceanic and Atmospheric Administration (NOAA). The ERA-5 data were obtained from http://www.ecmwf.int. The sea surface current and sea-level data from HYCOM were openly accessed from https://www.hycom.org. The General Bathymetric Chart of the Oceans bathymetry data were downloaded from ftp.edcftp.cr.usgs.gov. The rainfall observations and the information about hurricane's best tracks were

collected by the Stepped-Frequency Microwave Radiometers on board NOAA aircraft. The Haiyang-2B (HY-2B) data were provided by the National Satellite Ocean Application Service through an authorized account via https://osdds.nsoas.org.cn. The rain data from the Tropical Rainfall Measuring Mission were obtained via ftp.trmmopen.gsfc.nasa.gov and the typhoon parameters were provided by the Japan Meteorological Agency via http://www.jma.go.jp.

APPENDIX

TABLE II
COEFFICIENTS OF CRAIN_S1, IN WHICH THE SUBSCRIPTS 1, 2, AND 3 REPRESENT THE VARIABLES σ_D, θ, AND U_{10}, E.G., A12 IS THE COEFFICIENT FOR THE TERM $\sigma_D \times \theta$

θ	Coefficient	Within 100 km Beyond 100 km	Coefficient	Within 100 km Beyond 100 km
30°–35°	a_0	−645.890310 −638.564623	a_{12}	0.368654 43.225701
	a_1	−5.797538 −26.950895	a_{13}	0.023329 0.096658
	a_2	2325.151176 2356.257817	a_{22}	−2003.141371 −1854.805631
	a_3	2.292281 9.634773	a_{23}	−3.240010 −25.262095
	a_{11}	0.193670 −0.004836	a_{33}	−0.008206 0.043568
35°–40°	a_0	181.160551 −163.053525	a_{12}	−46.522698 3.578392
	a_1	19.937171 2.668373	a_{13}	0.016103 −0.114136
	a_2	−1192.341606 450.673060	a_{22}	1625.110379 −448.959417
	a_3	3.381949 0.383494	a_{23}	−5.483178 2.488887
	a_{11}	0.273820 −0.058868	a_{33}	−0.001878 −0.004277
40°–45°	a_0	723.057942 −858.648628	a_{12}	−30.592918 25.812015
	a_1	47.350812 4.059206	a_{13}	−0.176395 −0.260024
	a_2	−3070.779582 2344.602790	a_{22}	2454.461426 −2063.448046
	a_3	2.325848 3.381523	a_{23}	1.911503 2.539705
	a_{11}	−0.778853 −0.494720	a_{33}	−0.018257 −0.023876
45°–50°	a_0	/ 222842.161672	a_{12}	/ −113.611831
	a_1	/ 86.974659	a_{13}	/ 0.092513
	a_2	/ −626855.11	a_{22}	/ 440892.78
	a_3	/ 50.140779	a_{23}	/ −76.434974
	a_{11}	/ −0.331067	a_{33}	/ 0.048939

REFERENCES

[1] E. L. Harrison, F. Veron, D. T. Ho, M. C. Reid, P. Orton, and W. R McGillis, "Nonlinear interaction between rain- and wind-induced air-water gas exchange," *J. Geophys. Res., Oceans*, vol. 117, no. C3, Mar. 2012, Art. no. C03034.

[2] Y. Q. Wang, Y. Q. Wang, and H. Fudeyasu, "The role of Typhoon Songda (2004) in producing distantly located heavy rainfall in Japan," *Monthly Weather Rev.*, vol. 137, no. 11, pp. 3699–3716, Nov. 2009.

[3] K. M. Lau and Y. P. Z. William, "Observed recent trends in tropical cyclone rainfall over the North Atlantic and the North Pacific," *J. Geophys. Res., Atmos.*, vol. 117, no. D3, Feb. 2012, Art. no. D03104.

[4] R. J. Watson, A. R. Holt, V. Marecal, and J. Testud, "A rainrate-attenuation-reflectivity relation for use in the spaceborne and airborne sensing of rain," *IEEE Trans. Geosci. Remote Sens.*, vol. 37, no. 3, pp. 1447–1450, May 1999.

[5] C. Kummerow, W. Barnes, T. Kozu, J. Shiue, and J. Simpson, "The Tropical Rainfall Measuring Mission (TRMM) sensor package," *J. Atmos. Ocean. Technol.*, vol. 15, no. 3, pp. 809–817, Jun. 1998.

[6] T. Zhang, S. Quan, Z. Yang, Z. Zhang, W. Guo, and H. Gan, "A two-stage ship detection scheme for PolSAR image," *IEEE Trans. Geosci. Remote Sens.*, vol. 60, 2022, Art. no. 5236918.

[7] W. Z. Shao, X. M. Li, S. Lehner, and C. L. Guan, "Development of polarization ratio model for sea surface wind field retrieval from Terrasar-X HH polarization data," *Int. J. Remote Sens.*, vol. 35, no. 11/12, pp. 4046–4063, Jul. 2014.

[8] S. Zhu, W. Z. Shao, and X. Z. Yuan, "Semi-empirical algorithm for wind speed retrieval from Gaofen-3 quad-polarization strip mode SAR data," *J. Ocean Univ. China*, vol. 19, no. 1, pp. 23–35, Feb. 2020.

[9] W. R. Alpers, D. B. Ross, and C. L. Rufenach, "On the detectability of ocean surface waves by real and synthetic aperture radar," *J. Geophys. Res., Oceans*, vol. 86, pp. 6481–6498, Jul. 1981.

[10] H. Masuko, K. Okamoto, M. Shimada, and S. Niwa, "Measurement of microwave backscattering signatures of the ocean surface using X band and Ka band airborne scatterometers," *J. Geophys. Res., Oceans*, vol. 91, no. C11, pp. 13065–13083, Nov. 1986.

[11] H. Hersbach, "Comparison of C-band scatterometer CMOD5.N equivalent neutral winds with ECMWF," *J. Atmos. Ocean. Technol.*, vol. 27, no. 4, pp. 721–736, Apr. 2010.

[12] X.-M. Li and S. Lehner, "Algorithm for sea surface wind retrieval from TerraSAR-X and TanDEM-X data," *IEEE Trans. Geosci. Remote Sens.*, vol. 52, no. 5, pp. 2928–2939, May 2014.

[13] O. Isoguchi and M. Shimada, "An L-band ocean geophysical model function derived from PALSAR," *IEEE Trans. Geosci. Remote Sens.*, vol. 47, no. 7, pp. 1925–1936, Jul. 2009.

[14] P. A. Hwang and F. Fois, "Surface roughness and breaking wave properties retrieved from polarimetric microwave radar backscattering," *J. Geophys. Res., Oceans*, vol. 120, no. 5, pp. 3640–3657, May 2015.

[15] W. Z. Shao, Y. Y. Hu, F. Nunziata, V. Corcione, M. Migliacciom, and X. M. Li, "Cyclone wind retrieval based on X-band SAR-derived wave parameter estimation," *J. Atmos. Ocean. Technol.*, vol. 37, no. 10, pp. 1907–1924, Oct. 2020.

[16] B. Zhang and W. Perrie, "Cross-polarized synthetic aperture radar: A new potential technique for hurricanes," *Bull. Amer. Meteorol. Soc.*, vol. 93, no. 4, pp. 531–541, Apr. 2012.

[17] W. Z. Shao et al., "Analysis of wave distribution simulated by WAVEWATCH-III model in typhoons passing Beibu Gulf, China," *Atmosphere*, vol. 9, no. 7, Jul. 2018, Art. no. 265.

[18] D. E. Weissman, M. A. Bourassa, and J. Tongue, "Effects of rain rate and wind magnitude on sea winds scatterometer wind speed errors," *J. Atmos. Ocean. Technol.*, vol. 19, no. 5, pp. 738–746, May 2002.

[19] M. P. Owen and D. G. Long, "Prior selection for QuikSCAT ultra-high-resolution wind and rain retrieval," *IEEE Trans. Geosci. Remote Sens.*, vol. 51, no. 3, pp. 1555–1567, Mar. 2013.

[20] M. P. Owen and D. G. Long, "Simultaneous wind and rain estimation for QuikSCAT at ultra-high resolution," *IEEE Trans. Geosci. Remote Sens.*, vol. 49, no. 6, pp. 1865–1878, Jun. 2011.

[21] M. A. Bourassa et al., "Remotely sensed winds and wind stresses for marine forecasting and ocean modeling," *Front. Mar. Sci.*, vol. 6, no. 8, Aug. 2019, Art. no. 443.

[22] M. Migliaccio, P. Lecomte, G. D. Chiara, and R. Crapolicchio, "ERS C-band scatterometer and tropical cyclone observation," *Rivista Ital. Telerilevamento*, vol. LVIII, no. 1, pp. 143–151, Jan. 2003.

[23] V. Corcione, F. Nunziata, and M. Migliaccio, "Megi typhoon monitoring by X-band synthetic aperture radar measurements," *IEEE J. Ocean. Eng.*, vol. 43, no. 1, pp. 184–194, Jan. 2018.

[24] K. Hasselmann and S. Hasselmann, "On the nonlinear mapping of an ocean wave spectrum into a synthetic aperture radar image spectrum and its inversion," *J. Geophys. Res., Oceans*, vol. 96, no. C6, pp. 10713–10729, Jun. 1991.
[25] C. Mastenbroek and C. F. de Valk, "A semiparametric algorithm to retrieve ocean wave spectra from synthetic aperture radar," *J. Geophys. Res., Oceans*, vol. 105, no. C2, pp. 3497–3516, Feb. 2000.
[26] W. Z. Shao, X. W. Jiang, Z. F. Sun, Y. Y. Hu, A. Marino, and Y. G. Zhang, "Evaluation of wave retrieval for Chinese Gaofen-3 synthetic aperture radar," *Geo-Spatial Inf. Sci.*, vol. 25, no. 2, pp. 229–243, Mar. 2022.
[27] J. Schulz-Stellenfleth, T. Konig, and S. Lehner, "An empirical approach for the retrieval of integral ocean wave parameters from synthetic aperture radar data," *J. Geophys. Res., Oceans*, vol. 112, no. C3, Mar. 2007, Art. no. C03109.
[28] Y. X. Sheng et al., "Validation of significant wave height retrieval from co-polarization Chinese Gaofen-3 SAR imagery using an improved algorithm," *Acta Oceanology Sinica*, vol. 37, no. 6, pp. 1–10, Jun. 2018.
[29] P. G. Black, V. J. Cardone, R. C. Gentry, and J. D. Hawkins, "Chapter 6 Seasat microwave wind and rain observations in severe tropical and midlatitude marine storms," *Adv. Geophys.*, vol. 27, no. 1985, pp. 197–277, Jan. 1985.
[30] C. Melsheimer, W. Alpers, and M. Gade, "Investigation of multifrequency/multipolarization radar signatures of rain cells over the ocean using SIC-C/X-SAR data," *J. Geophys. Res., Oceans*, vol. 103, no. C9, pp. 18867–18884, May 1996.
[31] D. Atlas and P. G. Black, "The evolution of convective storms from their footprints on the sea as viewed by synthetic aperture radar from space," *Bull Amer. Meteorol. Soc.*, vol. 75, no. 7, pp. 1183–1190, Jul. 1994.
[32] A. R. Jameson et al., "SIR-C/X-SAR observations of rain storms," *Remote Sens. Environ.*, vol. 59, no. 2, pp. 267–279, Feb. 1997.
[33] C. Melsheimer, W. Alpers, and M. Gade, "Simultaneous observations of rain cells over the ocean by the synthetic aperture radar aboard the ERS satellites and by surface-based weather radars," *J. Geophys. Res., Oceans*, vol. 106, no. C3, pp. 4665–4677, Mar. 2001.
[34] C. Nie and D. G. Long, "A C-band scatterometer simultaneous wind/rain retrieval method," *IEEE Trans. Geosci. Remote Sens.*, vol. 46, no. 11, pp. 3618–3631, Nov. 2008.
[35] C. Nie and D. G. Long, "A C-band wind/rain backscatter model," *IEEE Trans. Geosci. Remote Sens.*, vol. 45, no. 3, pp. 621–631, Mar. 2007.
[36] F. Xu, W. Perrie, B. Toulany, and P. C. Smith, "Wind-generated waves in hurricane Juan," *Ocean Model.*, vol. 163, no. 3, pp. 188–205, 2007.
[37] I. I. Lin, W. Alpers, V. Khoo, H. Lim, T. K. Lim, and D. Kasilingam, "An ERS-1 synthetic aperture radar image of a tropical squall line compared with weather radar data," *IEEE Trans. Geosci. Remote Sens.*, vol. 39, no. 5, pp. 937–945, May 2001.
[38] W. Alpers, C. M. Cheng, Y. Shao, and L. M. Yang, "Study of rain events over the South China sea by synergistic use of multi-sensor satellite and ground-based meteorological data," *Photogramm. Eng. Remote Sens.*, vol. 73, no. 3, pp. 267–278, Mar. 2007.
[39] X. B. Zhao, W. Z. Shao, L. B. Zhao, Y. Gao, Y. Y. Hu, and X. Z. Yuan, "Impact of rain on wave retrieval from sentinel-1 synthetic aperture radar images in tropical cyclones," *Adv. Space Res.*, vol. 67, no. 10, pp. 3072–3086, May 2021.
[40] M. Gade, W. Alpers, H. Huhnerfuss, H. Masuko, and T. Kobayashi, "Imaging of biogenic and anthropogenic ocean surface films by the multifrequency/multipolarization SIR-C/X-SAR," *J. Geophys. Res., Oceans*, vol. 103, no. C9, pp. 18851–18866, Aug. 1998.
[41] V. N. Kudryavtsev, B. Chapron, A. G. Myasoedov, F. Collard, and J. A. Johannessen, "On dual co-polarized SAR measurements of the ocean surface," *IEEE Geosci. Remote Sens. Lett.*, vol. 10, no. 4, pp. 761–765, Jul. 2013.
[42] Z. F. Sun et al., "Contribution of breaking wave on the co-polarized backscattering measured by the Chinese Gaofen-3 SAR," *Int. J. Remote Sens.*, vol. 43, no. 4, pp. 1384–1408, Feb. 2022.
[43] H. L. Tolman, "A third-generation model for wind waves on slowly varying, unsteady, and inhomogeneous depths and currents," *J. Phys. Oceanogr.*, vol. 21, no. 6, pp. 782–797, Jun. 1991.
[44] Y. Y. Hu, W. Z. Shao, J. Shi, J. Sun, Q. Y. Ji, and L. N. Cai, "Analysis of the typhoon wave distribution simulated in WAVEWATCH-III model in the context of Kuroshio and wind-induced current," *J. Oceanol. Limnol.*, vol. 38, no. 6, pp. 1692–1710, Nov. 2020.
[45] W. J. Plant, "A stochastic, multiscale model of microwave backscatter from the ocean," *J. Geophys. Res., Oceans*, vol. 107, no. C9, pp. 3-1–3-21, Sep. 2002.
[46] R. Romeiser, W. Alpers, and V. Wismann, "An improved composite surface model for the radar backscattering cross section of the ocean surface: 1. Theory of the model and optimization/validation by scatterometer data," *J. Geophys. Res., Oceans*, vol. 102, no. C11, pp. 25237–25250, Nov. 1997.
[47] V. N. Kudryavtsev, S. Fan, B. Zhang, A. A. Mouche, and B. Chapron, "On quad-polarized SAR measurements of the ocean surface," *IEEE Trans. Geosci. Remote Sens.*, vol. 57, no. 11, pp. 8362–8370, Nov. 2019.
[48] Y. Gao, C. L. Guan, J. Sun, and L. Xie, "A new hurricane wind direction retrieval method for SAR images without hurricane eye," *J. Atmos. Ocean. Technol.*, vol. 35, no. 11, pp. 2229–2239, Nov. 2018.
[49] J. E. Kim and M. J. Alexander, "Tropical precipitation variability and convectively coupled equatorial waves on submonthly time scales in reanalyses and TRMM," *J. Climate*, vol. 26, no. 10, pp. 3013–3030, May 2013.
[50] G. S. Zhang, X. F. Li, W. Perrie, B. Zhang, and W. Lei, "Rain effects on the hurricane observations over the ocean by C-band synthetic aperture radar," *J. Geophys. Res., Oceans*, vol. 121, no. 1, pp. 14–26, Jan. 2016.
[51] Z. H. Yang, W. Z. Shao, Y. Ding, J. Shi, and Q. Y. Ji, "Wave simulation by the SWAN model and FVCOM considering the sea-water level around the Zhoushan islands," *J. Mar. Sci. Eng.*, vol. 8, no. 10, Oct. 2020, Art. no. 783.
[52] S. Abdalla, "Are Jason-2 significant wave height measurements still useful," *Adv. Space Res.*, vol. 68, no. 2, pp. 802–807, Jun. 2021.
[53] W. Shao, T. Jiang, X. Jiang, Y. Zhang, and W. Zhou, "Evaluation of sea surface winds and waves retrieved from the Chinese HY-2B data," *IEEE J. Sel. Topics Appl. Earth Observ. Remote Sens.*, vol. 14, pp. 9624–9635, 2021.
[54] R. Yao, W. Z. Shao, X. W. Jiang, and T. Yu, "Wind speed retrieval from the Chinese Gaofen-3 synthetic aperture radar using an analytical approach in the nearshore waters of China's seas," *Int. J. Remote Sens.*, vol. 43, no. 8, pp. 3028–3048, Apr. 2022.
[55] T. Xie, S. Z. Zhao, W. Perrie, H. Fang, W. J. Yu, and Y. J. He, "Electromagnetic backscattering from one-dimensional drifting fractal sea surface I: Wave–current coupled model," *Chin. Phys. B*, vol. 25, no. 6, pp. 214–219, Jun. 2016.
[56] R. D. Viana, J. A. Lorenzzetti, J. T. Carvalho, and F. Nunziata, "Estimating energy dissipation rate from breaking waves using polarimetric SAR images," *Sensors*, vol. 20, no. 22, Nov. 2020, Art. no. 6540.
[57] W. Alpers and B. Brümmer, "Atmospheric boundary layer rolls observed by the synthetic aperture radar aboard the ERS-1 satellite," *J. Geophys. Res.*, vol. 99, no. C6, pp. 12613–12621, Jun. 1994.
[58] A. Pleskachevsky, S. Jacobsen, B. Tings, and E. Schwarz, "Estimation of sea state from Sentinel-1 synthetic aperture radar imagery for maritime situation awareness," *Int. J. Remote Sens.*, vol. 40, no. 11, pp. 4104–4142, Jan. 2019.
[59] M. D. Powell, "The transition of the hurricane frederic boundary-layer wind field from the open gulf of Mexico to landfall," *Monthly Weather Rev.*, vol. 110, no. 12, pp. 1912–1932, Dec. 1982.
[60] H. Shen, C. Seitz, W. Perrie, Y. J. He, and M. Powell, "Developing a quality index associated with rain for hurricane winds from SAR," *Remote Sens.*, vol. 10, no. 11, Nov. 2018, Art. no. 1783.
[61] J. Shi et al., "The impact of rain to observed signal from Chinese Gaofen-3 synthetic aperture radar in typhoons," *Acta Oceanol. Sinica*, vol. 38, no. 11, pp. 121–133, Nov. 2019.

Xianbin Zhao received the Ph.D. degree in atmospheric detection theory and technology from PLA University of Science and Technology, Beijing, China, in 2015.

He is mainly engaged in the research and teaching of synthetic aperture radar ocean remote sensing. He has published a number of papers in the field of ocean surface wind field and wave retrieval. He is concerned about the impact of precipitation on synthetic aperture radar of ocean sounding. He is currently a Lecturer with the College of Meteorology and Oceanography, National University of Defense Technology, Changsha, China.

Weizeng Shao (Member, IEEE) received the B.S. degree in engineering from Jiangsu University of Science and Technology, Zhenjiang, China, in 2007, and the Ph.D. degree in physical oceanography from the Ocean University of China, Qingdao, China, in 2013.

During his Ph.D. program during 2010–2012, he was a Visiting Research Scientist with the SAR oceanography group at the German Aerospace Center (DLR), Munich, Germany. During 2015−2020, he was an Associate Professor and a Master's student supervisor with Zhejiang Ocean University, Zhoushan, China. His research has focused on the marine applications using synthetic aperture radar, especially for Chinese GF-3, HY-2, and CFOSAT, and ocean modeling for typhoons and hurricanes. Since 2019, he has been an Assistant Researcher with the National Satellite Ocean Application Service, Beijing, China. Since 2021, he has been a Full Professor with Shanghai Ocean University, Shanghai, China.

Zhengzhong Lai received the B.S. degree in marine fisheries science and technology from Dalian Ocean University, Dalian, China, in 2016. He is currently working toward master's degree in physical oceanography from Shanghai Ocean University, Shanghai, China.

His research interests include remote sensing and marine simulations based on the numeric models.

Xingwei Jiang received the Ph.D. degree in physical oceanography from Ocean University of China, Qingdao, China, in 2008.

He became an Academician with the Chinese Academy of Engineering and a Doctoral Supervisor. He presided over the establishment of a marine satellite ground application system platform and formulated marine remote sensing technical regulations. He was the Vice Chairman of the Chinese Ocean Society and the China Association of Remote Sensing Applications. He was the Chairman of the Ocean Remote Sensing Professional Committee of the Chinese Ocean Society and a member of the International GEO Organization Technical Coordination Group and the Sino-French Marine Satellite Joint Steering Committee. He has published a number of monographs, atlases, and papers, and formed a marine satellite ground application engineering technical team. He is currently the Director of the Chinese National Satellite Marine Application Center and a Chief Designer of Chinese marine satellite ground application systems.